



UKAEA-CCFE-PR(25)363

Bin Zhu, Omar Mohamed, Abdalrhaman Koko, Hannah Zhangb, Jiří Dluhoš, Yiqiang Wang, Michael Gorley, Mark J. Whiting, Tan Sui

Revealing residual stress and hightemperature mechanical performance of laser-welded P91 steel for fusion power plant components

Enquiries about copyright and reproduction should in the first instance be addressed to the UKAEA Publications Officer, Culham Science Centre, Building K1/0/83 Abingdon, Oxfordshire, OX14 3DB, UK. The United Kingdom Atomic Energy Authority is the copyright holder.
The contents of this document and all other UKAEA Preprints, Reports and Conference Papers are available to view online free at scientific-publications.ukaea.uk/

Revealing residual stress and hightemperature mechanical performance of laser-welded P91 steel for fusion power plant components

Bin Zhu, Omar Mohamed, Abdalrhaman Koko, Hannah Zhangb, Jiří Dluhoš, Yiqiang Wang, Michael Gorley, Mark J. Whiting, Tan Sui

Revealing residual stress and high-temperature mechanical performance of laserwelded P91 steel for fusion power plant components

Bin Zhu^a, Omar Mohamed^a, Abdalrhaman Koko^b, Hannah Zhang^b, Jiří Dluhoš^c, Yiqiang Wang^d, Michael Gorley^d, Mark J. Whiting^a, Tan Sui^{a,b}*

Corresponding email address: t.sui@surrey.ac.uk

 $[^]a$ School of Mechanical Engineering Sciences, University of Surrey, Guildford, Surrey, GU2 7XH, UK

^b National Physical Laboratory, Hampton Road, Teddington TW11 0LW, UK

^c TESCAN ORSAY HOLDING, a.s., Libušina třída 21, 623 00 Brno, Czech Republic

^d United Kingdom Atomic Energy Authority, Culham Centre for Fusion Energy, Culham Science Centre, Abingdon, Oxon, OX14 3DB, UK

Abstract

The extreme working conditions of the in-vessel components in nuclear fusion reactors require remote laser-welding for maintenance. However, this process induces heterogeneous residual stress, which can interact with microstructures, degrading mechanical properties. Involving the high-temperature operating environment can further sophisticate the degradation. Here, the residual stress distribution of laser-welded P91 joints was evaluated, where the peak residual tensile stress (~ 150 MPa) is observed at the fusion zone and heat affected zone (FZ/HAZ) interface, whereas the highest compressive stress (~550 MPa) is located at HAZ and base material interface. The correlation between microstructures, fractography, residual stresses and mechanical properties was established to investigate deformation mechanism at room and high temperatures. While the microstructural strengthening phenomenon is overwhelming in tension, residual stress effect in micro-hardness is much identical. The results provide insight into maintaining structural integrity for this critical engineering challenge.

Keywords: laser-welded P91 joints; deformation mechanism; residual stress; PFIB-DIC; nanoindentation;

Impacts statement: Deformation mechanism of laser-welded P91 joints is investigated by comprehensive considering residual stresses and microstructures to enhance understanding in maintaining the structural integrity for nuclear fusion power plant components.

1. Introduction

To solve the relentless upward march in energy demands and the rise of energy-related emissions, a shift towards sustainable, clean energy production is more imperative than ever before. Nuclear fusion is a seemingly attractive option to the demand and, if viable, provides an abundance of benefits unmatched by other solutions currently being explored. The demanded technologies are not only for controlling a more robust plasma than previously existed but also for safely generating electricity consistently and for regular, rapid, and reliable maintenance of the plant.

The in-vessel components in the fusion/fission plant such as pipes for heat exchangers and helium and coolants, have to utilise complex materials systems and complicated joining techniques to maintain their function under high-temperature operating conditions, up to 650 °C [1–4]. P91 steel, denoted ASTM A335 for plate and T91 for tubing, is renowned for its excellent high-temperature properties, in particular, high-temperature creep resistance and oxidation resistance. An attractive quality of P91 is the weldability and microstructural stability at elevated temperatures for extensive periods [5]. Laser welding has been investigated as one of the most promising joint techniques to produce these pipes, which has been previously proved by using remote laser tools to butt-weld in-vessel components [6,7]. However, substantial microstructural changes and induced heterogeneous residual stress of the weldment notably affects the mechanical properties. Such effect can be more sophisticated, rendering the mechanical properties unpredictable at the high operating temperature. It is critical to investigate the deformation mechanism and reveal the mechanical properties at both room and high temperature for maintaining the structural integrity of the laser-welded joints [8,9].

Several studies have been achieved on analysing the mechanistic connection of microstructures with micro-hardness distribution and tensile strength [10–14]. The change of the micro-hardness has been correlated with hardening effects of recrystalisation, precipitates and martensitic phase transformation originated from high heat input during laser welding. Additionally, using digital image correlation to monitor the strain evaluation during tensile deformation allows the study of tensile behaviour in local sub-regions and builds correlation with localised microstructures [15,16]. However, the heterogeneous residual stress effects have been overlooked for a comprehensive deformation mechanism within the laser-welded P91 joints.

Quantitative evaluation of the residual stress in narrow sub-regions of the weldment is critical for assessing its relationship to strength degradation and the deformation mechanism.

This requires reliable residual stress measurements on the microscale. Current residual stress measurements at the microscale includes lab-based and synchrotron-based X-ray diffraction techniques that usually require thin sample dimensions due to their intrinsic penetration limitation [17–20]. The residual stress leans towards releasing during the thin sample preparation, resulting in unexpected uncertainties. The residual stress evaluation for similar or dissimilar P91 joints has been primarily conducted using the contour method, neutron diffraction and finite element analysis (FEA) technique at a milimetre scale [21–26]. However, the residual stress on a finer scale, which is profound in correlating the heterogeneous mechanical properties for the narrow sub-regions of the laser-welded P91 joint, has not been revealed.

This study applied a novel tunable-scale residual stress evaluation technique, which is known as plasma focused ion beam and digital image correlation (PFIB-DIC) technique [27], to quantify residual stress across narrow sub-regions of the laser-welded P91 joints, i.e., fusion zone (FZ), heat-affected zone (HAZ), base material (BM). Instrumented nanoindentation was also used to cross-validate the residual stress distribution and characterise the micro-hardness. The microstructural changes over the weldment are then observed by the electron backscatter diffraction (EBSD). Whilst the overall tensile behaviours are evaluated at both room and high temperatures and the local heterogenous tensile strain evolution in different sub-regions is characterised by the DIC at room temperature. The influence of heterogeneous microstructural and residual stress distribution on mechanical properties is quantitatively analysed with respect to the micro-hardness and tensile strength difference in FZ, HAZ and BM regions. The investigation provides insights into establishing high-precision predictive tools for the lifespan of fusion power plant components to improve the service time.

2. Materials and Methods

The P91 steel with a composition Fe-0.12C-8.32Cr-1.02Mo-0.41Mn-0.24V (in weight %) was used in the present investigation. The as-received 6-mm-thick P91 steel plate was normalised at $1050\,^{\circ}$ C, and water quenched to room temperature followed by tempering at 760 °C then cooled in the air [13]. The laser-welded P91 plate was butt welded perpendicular to the rolling direction by two as-received P91 steel plates, each $150\times75\times6$ mm³. The single-pass laser welding using a 5 kW Yb-fibre laser source with a welding speed of 1.2 m/min was employed at The Welding Institute (TWI), achieving a fully penetration, narrow FZ and HAZ, and a slightly concave shape weldment. As shown in **Fig. 1**(a), the laser-welded P91 specimen

used in this research was cut from the laser-welded P91 plate by electrical discharge machining with the dimension of $\sim 25 \times 6 \times 6$ mm³. The microstructures characterisation was carried out in the red box (**Fig. 1**(a)) by a Jeol-7100F field emission scanning electron microscopy (SEM), equipped with a Thermo Fisher Lumis EBSD detector. Post-data-treatment was completed with MTEX 5.2.8 [28], and the crystal size was measured by the mean linear intercept method [29]. The material anisotropy in x and y directions, i.e. Young's modulus and Poisson's coefficient, was reckoned according to the crystal orientation.

The PFIB-DIC ring-core method was applied in the FZ, HAZ and BM regions, as well as the interface of FZ/HAZ and HAZ/BM (**Fig. 1**(a)) to assess the non-euqi-biaxial residual stresses because it allows simultaneous evaluation of three components of in-plane normal and shear strain relaxation ($\Delta \varepsilon_x$, $\Delta \varepsilon_y$ and $\Delta \varepsilon_{xy}$), as shown in **Fig. 1**(b) [27,30]. Considering anisotropic properties of ring-cores, the residual stresses in x and y directions was calculated by using the generalised Hooke's law (**Eq. 1** and **Eq. 2**) [27,31]. The derivation of the three strain components and in-plane residual stress components enable direct determination of the principal residual stresses using Mohr's circle [32].

$$\sigma_{x}^{PFIB} = -\frac{E_{x}}{(1 - v_{x}v_{y})} \left[\Delta \varepsilon_{\infty}^{x} + v_{x} \Delta \varepsilon_{\infty}^{y} \right]$$
 Eq. 1

$$\sigma_y^{PFIB} = -\frac{E_y}{(1 - v_x v_y)} \left[\Delta \varepsilon_{\infty}^{y} + v_y \Delta \varepsilon_{\infty}^{x} \right]$$
 Eq. 2

where $\Delta \varepsilon_{\infty}^{\mathbf{x}}$ and $\Delta \varepsilon_{\infty}^{\mathbf{y}}$ are the strain relaxations, and σ_{x}^{PFIB} and σ_{y}^{PFIB} are two in-plane residual stress components in x and y directions. E_{x} , E_{y} , v_{x} , and v_{y} are Young's modulus and Poisson's coefficients computed according to the crystal orientation in the ring-core area in x and y directions, respectively.

Fig. 1(c) schematically shows how nanoindentation is used to measure the residual stress in weldment by comparing the load-displacement curve with the stress-free reference obtained from the ring-core regions. The classical symmetric pyramid or spherical indenter tip limits the use of nanoindentation in non-equi-biaxial residual stress states. Using the PFIB-DIC technique allows the determination of a pre-known stress ratio between two principal residual stress components (σ_1^{PFIB} and σ_2^{PFIB}) to estimate non-equi-biaxial residual stress via Lee's model [27,33,34]. The high-resolution stress ratio was gained from PFIB-DIC measurements using **Eq. 3**. The line-scan was performed across the weldment for residual stress and micro-hardness characterisation, as shown in **Fig. 1**(a). Depth-control with 1µm/min was used to carry out the indentation using Ultra Indentation Tester (UNHT), and results were considered at depths of

500 nm and 1000 nm. The area function of the Berkovich indenter was calibrated against the certified reference material. The Micro-hardness is determined according to the Oliver and Pharr theory [35].

$$k = \frac{\sigma_1^{PFIB}}{\sigma_2^{PFIB}} \ (-1 < k < 1 \ and \ k \neq 0)$$
 Eq. 3

where the σ_1^{PFIB} and σ_2^{PFIB} are the two principal residual stress components from the PFIB-DIC ring-core method.

The samples for the tensile testing, including dog-bone and rectangular shapes, were cut-off by electrical discharge machining from the same laser-welded P91 plate. The uniaxial tensile experiment at room temperature was conducted using a universal material testing machine (Instron 5500). The deformation is induced in uniaxial tension until failure at a constant displacement rate of 0.02 mm/s, and the DIC software (Vic-2D v6, Correlated Solutions, US) [36] was used to visualise the heterogeneous strain distribution throughout the tensile deformation. The tensile behaviours were characterised by multiple virtual extensometers, as shown in **Fig. 1**(d). The high-temperature tensile testing was carried out using the electrothermal mechanical testing (ETMT). A R-type thermocouple was affixed to the centre heat zone of the sample **Fig. 1**(d)), which is in the dimension $3 \times 1 \times 65$ mm³, for monitoring and controlling the temperature. The temperature of the sample was then elevated to 550 °C at a rate of 5 °C/s, followed by a stabilising period of 2 minutes. The uniaxial tensile deformation was induced at a displacement rate of 0.02 mm/s until fractured

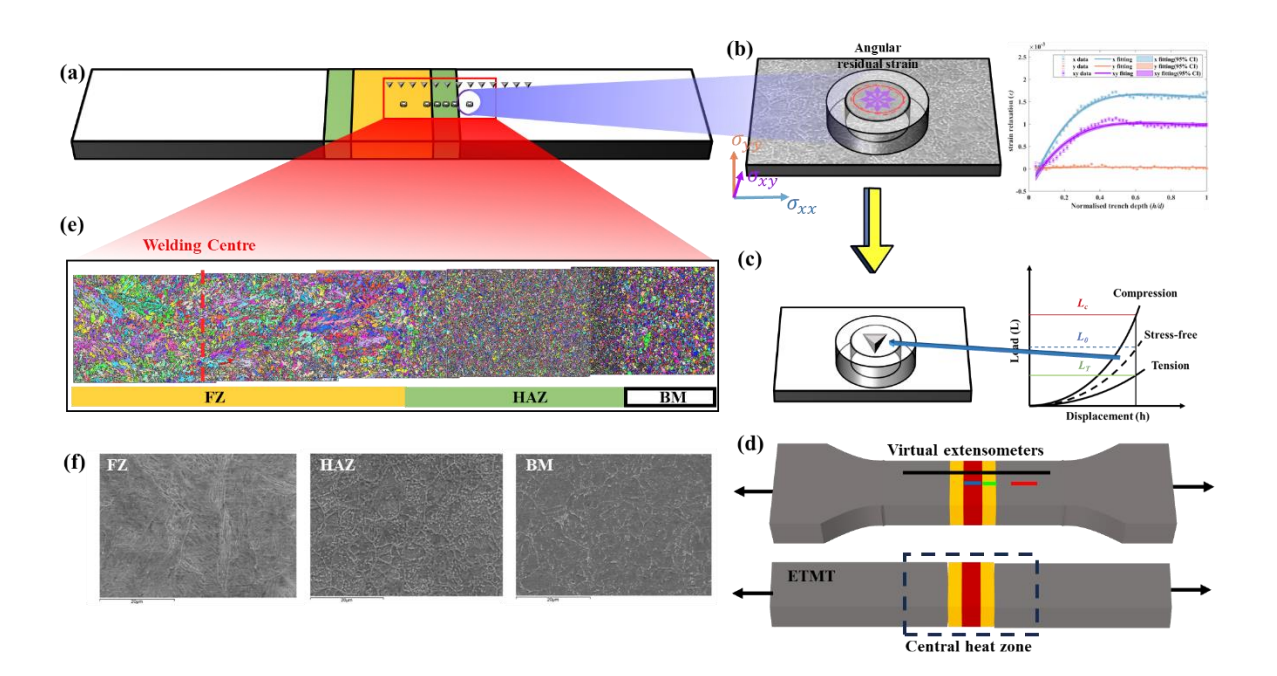


Fig. 1 (a) Laser-welded P91 specimen for residual stress, microstructures and micro-hardness characterisation. (b) Schematic figures illustrate the PFIB-DIC ring-core residual stress quantification. (c) Schematic figures show the nanoindentation residual stress measurement. The ring-core fabricated during PFIB-DIC measurement provides a stress-free reference. (d) The dog-bone specimen used in the room temperature uniaxial tensile experiment and virtual extensometers applied in DIC analysis. The rectangular sample for high-temperature tensile testing using the ETMT. (e) Stitched consecutive EBSD maps highlighted by the rectangle in red at (a). (f) Morphology characterisation at FZ, HAZ and BM regions, respectively.

3. Results and discussion

The stitched EBSD maps and SEM morphologies of the FZ, HAZ and BM regions shown in Fig. 1(e-f) exhibit the heterogeneous microstructural distribution across the weldment. The grain growth is observed in the FZ region, which is most evident close to the fusion line (FZ/HAZ interface). The grain size decreases dramatically from the FZ to HAZ, followed by a slight increase in the BM region. There is no obvious evidence showing the preferred orientation in the EBSD maps. The morphologies (Fig. 1(f)) varied substantially in the different areas across the weldment, depending on the peak heat input attained during the laser welding. Unlike other welding processes, the δ -ferrite, which is usually seen as an undesirable phase in 9-12% Cr steel, is not observed after laser-welding [37]. The quenched martensites are found in both FZ and HAZ regions, whereas the tempered martensite are identified in the HAZ and BM regions.

The PFIB-DIC ring-core method and nanoindentation techniques reveal residual stress distribution and build correlations with microstructures and mechanical properties. Fig. 2(a) shows an example of extracting the grain microstructures in the ring-core region from the EBSD map. The as-welded P91 steel is assumed to exhibit cubic crystal symmetry, and elastic constants of RAFM steel have been studied previously [38]. The anisotropic Young's modulus and Poisson's coefficient are computed circularly and used to calculate residual stress in x and y directions via generalised Hooke's law. Fig. 2(b) presents the residual stress distribution quantified by the PFIB-DIC ring-core method in x and y directions. Our findings show the peak magnitude of residual stresses is at the FZ/HAZ and HAZ/BM interfaces, where the microstructures change dramatically. The tensile peak of residual stress (~150 MPa) is found at the FZ/HAZ interface in x direction, balanced by compressive residual stress on both sides. The compressive peak (550 MPa) is identical at the interface of HAZ and BM. The residual stress is gradually diminishing while moving away from the weldment. The residual stress distribution in laser-welded P91 is consistent with other similar laser-welded RAFM joints, which was also measured by the PFIB-DIC ring-core method [27]. The principal residual stress derived from PFIB-DIC is displayed in **Fig. 2**(c), showing σ_1^{PFIB} and σ_2^{PFIB} .

Instrumented nanoindentation has great potential in massive use of identifying residual stresses because of the time efficiency, simplicity of use and applicability from nano to macro scales [33,34,39-41]. Fig. 2(d) and (e) show the equi-biaxial principal residual stress distribution (σ_{equi}^{indent}) extracted at the depth of 500 nm and 1000 nm from the nanoindentation measurement, respectively. The two depth-resolved residual stress distributions are in a similar trend, while the magnitude is slightly higher at depth of 500 nm. The pre-known stress coefficient concluded from the PFIB-DIC measurement is used to calculate the non-equibiaxial components (σ_1^{indent} and σ_2^{indent}) from nanoindentation. The distribution trends derived from nanoindentation measurements cross-validate the ones from the PFIB-DIC evaluation, although an discrepancy arises in magnitude. Such a difference suggests the depth sensitivity in the nanoindentation residual stress measurement at shallow position. On the one hand, the indentation size effect originates from dislocation density and causes load amplification in the load-displacement curve at a smaller scale [42]. The accompanying magnification of residual stress occurs while comparing with the stress-free reference. Although increasing displacement in nanoindentation measurement may extenuate this issue (Fig. 2(e)), risks might be raised in terms of the pile-up phenomenon in some compressive residual stress areas, leading to an unexpected error in accounting contact area. In this case, further evaluation of the contact area might be requested. On the other hand, non-equilibrium micro-scale residual stress derived from the local anisotropic properties also contributes to the depth effects. Applying multiple or high-depth measurements is able to consider a larger number of grains, equilibrating the micro-scale residual stress and overcoming this limitation [27].

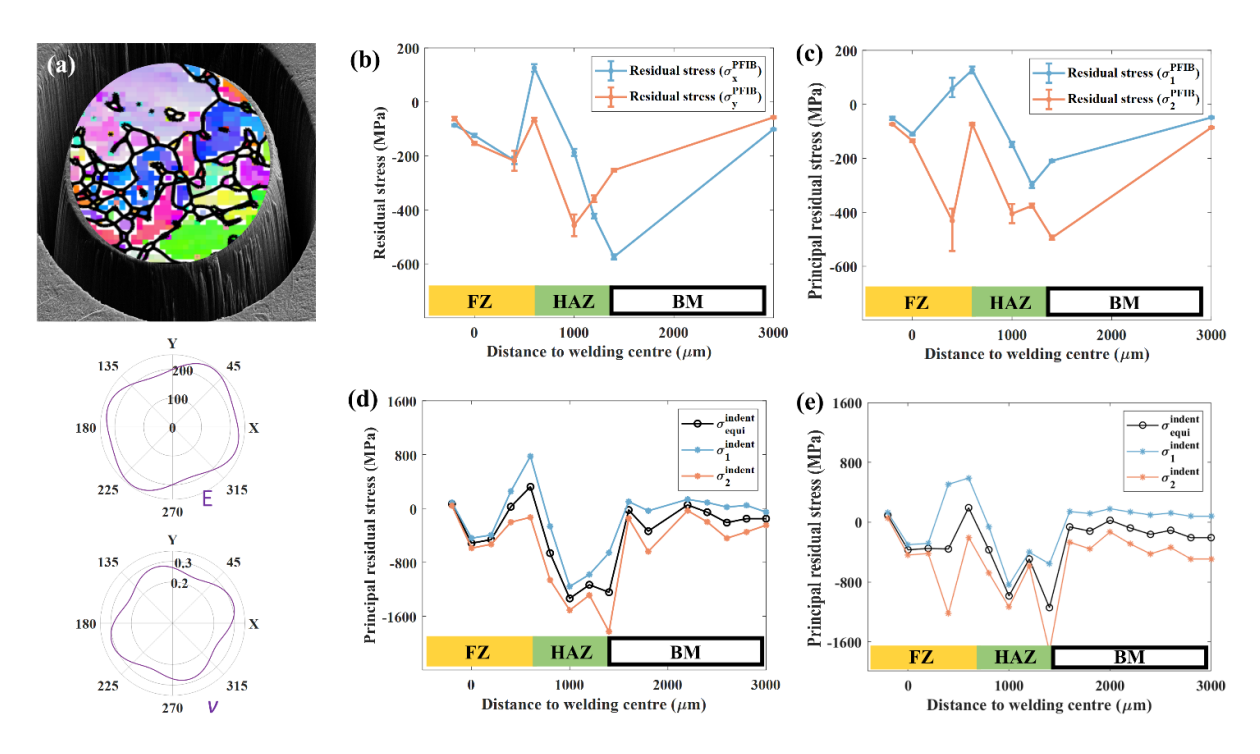


Fig. 2 Residual stress characterisation using PFIB-DIC ring-core method and nanoindentation technique with consideration of anisotropy. (a) EBSD map visualises the crystal orientation in the ring-core region by which the anisotropy is quantitatively calculated in x and y directions. (b) Residual stress distribution quantified by PFIB-DIC in x and y directions. (c) Principal residual stress distribution calculated from PFIB-DIC measurements. (d) Principal residual stress distribution analysed at depth of 500 nm using nanoindentation. (e) Principal residual stress distribution analysed at depth of 1000 nm using nanoindentation.

To study the residual stress effects on mechanical properties, the micro-hardness and tensile behaviour are characterised at room and high temperatures and visualised in **Fig. 3**. A significant advantage of using nanoindentation is that the micro-hardness and other mechanical properties can be measured in addition to residual stress measurements. Local micro-hardness values are severely affected by the microstructure (e.g., grain size, quenched martensite and precipitate) and the residual stress. The hardest position (~6.5 GPa) is identified in the HAZ, which is also adjacent to the fusion line (**Fig. 3**(a)). The micro-hardness gradually and constantly decreases to (~3.1 GPa) until the BM region. The microstructural hardening is concluded by comparing the micro-hardness of the stress-free reference ring-cores with that of the BM region. As shown in (**Fig. 3**(a)), the microstructures harden the edge of the FZ region up to ~5.9 GPa, which attributes to the quenched martensite and carbide dissolution during the welding cycle [43]. The grain growth (see **Fig. 1**(e)) in the FZ region slightly weakens this hardening effect. As the peak temperature decreases, the reduction of fraction of quenched martensite and residual of coarsen carbides decline the microstructure hardening in the HAZ region. Link to the residual stress distribution, the most apparent tensile principal residual stress

is located at the FZ region of the FZ/HAZ interface, which is due to the tensile residual stress tends to appear at the soft area [44,45]. The residual stress effects on micro-hardness is also separated quantitatively by comparing the micro-hardness between the as-welded state and stress-free reference in different regions of the weldment (**Fig. 3**(a)). The compressive residual stresses also hardens the FZ and HAZ regions, while the tensile residual stresses softening effect stands out around the fusion line. Both residual stress and microstructural hardening effects are diminishing while reaching the BM region, the micro-hardness almost remains the same as the parent materials.

Fig. 3(b) illustrates the tensile behaviour in the loading direction (*x* direction) at room and high temperatures, with the room temperature performance highlighted by a black rectangle. A detailed view is provided in **Fig. 3**(c). At the high temperature, the material exhibits a yield stress with a 0.2% offset of 345 MPa and an ultimate tensile stress (UTS) of 568 MPa. In contrast, at room temperature, the yield stress with a 0.2% offset is approximately 532 MPa, and the UTS is approximately 687 MPa. Compared to room temperature, the weldment demonstrates higher ductility and enhanced strain hardening effects at elevated temperatures.

The virtual extensometers covering different sub-regions enables the correlation between residual stress, microstructures and tensile behaviours at room temperature. As shown in Fig. **3**(c), the FZ region shows the highest yield stress (568 MPa) compared to the HAZ (539 MPa) and BM (504 MPa) regions. The resembling stiffness are found in the elastic regime for all global and sub-regions. Similar to the micro-hardness, the FZ region is the most strengthened region by microstructures (i.e. quenched martensite and carbide dissolution) and compressive residual stresses, while the BM region shows the highest ductility. The HAZ region is strengthened by its fine grain size, martensitic phase transformation and compressive residual stresses, where the yield strength is slightly below the FZ region. Fig. 3(c) also show the strain evolution at the UTS and after the necking while the sample is deformed in tension. The outstanding heterogeneous strain distribution is observed, and the strain is accumulated in the most ductile BM region, resulting in a fracture. The compressive residual stress aggressively hardens the HAZ region, which narrows the micro-hardness difference with the FZ region, whereas it unsuccessfully strengthens the HAZ region to reach the strength of the FZ region. This indicates that microstructural strengthening is dominated in tensile behaviours and residual stress hardening effects is more obvious than strengthening effects.

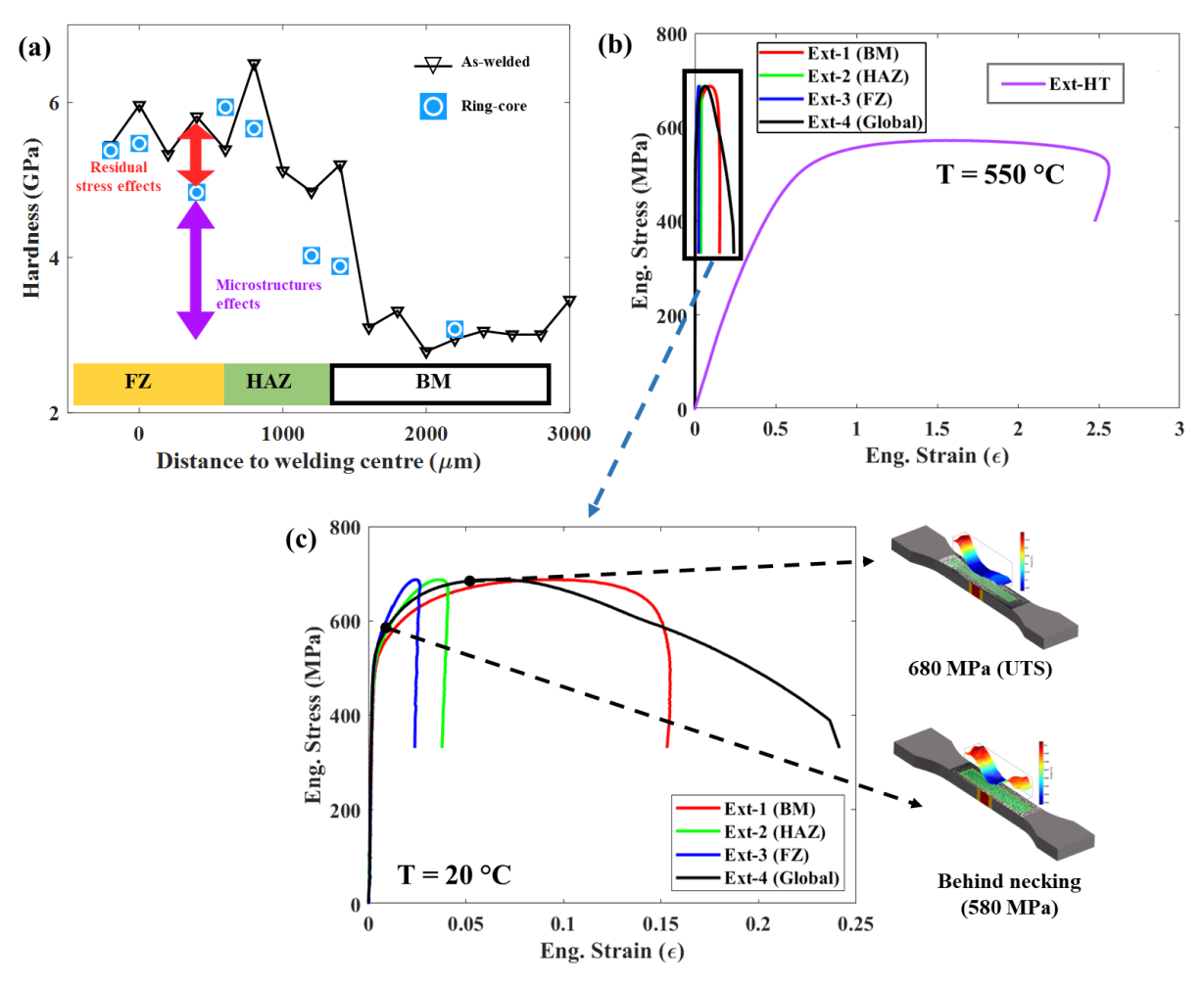


Fig. 3 Mechanical properties of as-welded and stress-free P91 steel at room and high temperatures. (a) Room-temperature evaluation of micro-hardness distribution across the weldment and stress-free ring-cores in the FZ, HAZ and BM regions. (b) Tensile behaviours at room and high-temperature of laser-welded P91 joint (c) Zoom-in figure for the tensile behaviours at room temperature measured by virtual extensometers and 2D maps of the strain evolution during the tensile deformation., which cover full gauge length, FZ, HAZ and BM regions, respectively.

At the room temperature, a mixed mode of ductile and brittle fracture is presented in **Fig. 4**(a). The ductile zones are represented by the presence of micro-voids and equiaxial dimples which embody the void growth and coalescence that eventually leads to the fracture. Large areas of quasi-cleavage facets are observed with River patterns, which are typical characteristics of transgranular brittle fracture [46]. Furthermore, the splitting and secondary cracking are also observed (**Fig. 4**(a)), which is due to the decohesion of interface between lath ferrite-lath matrix and secondary precipitates [47–49]. At the high temperature, the ductile fracture mode prevails, as depicted in **Fig. 4**(b), where the fracture surface exhibits ductile features, including dimples and micro- and macro-voids. In contrast to the room temperature fracture, which shows more cleavage features, the high-temperature fracture displays a limited number of cleavages, indicating a more ductile nature. This is also in good agreement with the

stress-strain graph (**Fig. 3**(b)) obtained where higher ductility and strain hardening effects is observed.

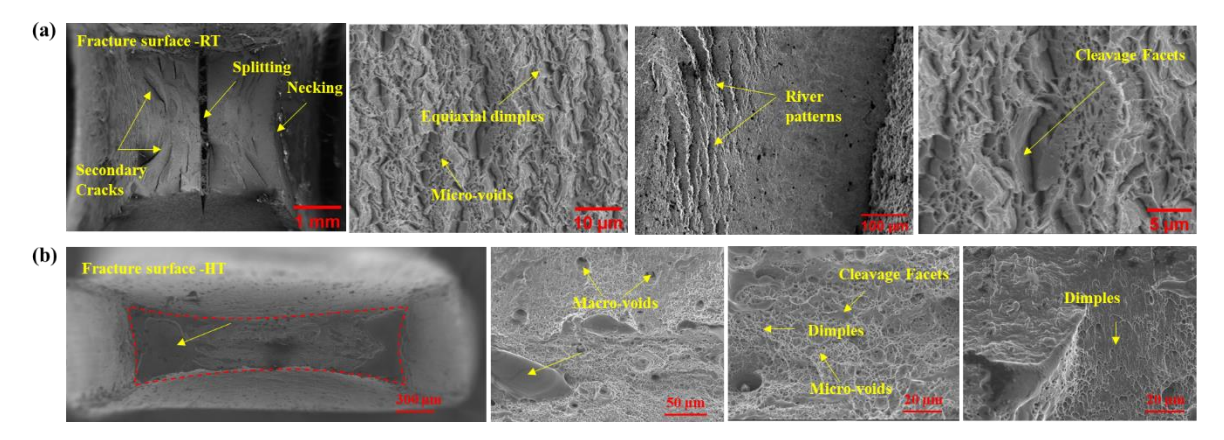


Fig. 4 The facture surfaces were characterised using SEM for the tensile testiong at (a) room temperature and (b) high temperature. Typical features of fractography were discovered, including splitting, secondary cracking and necking, dimples, micro(macro)-vioids, river patterns and Quasi clevage.

4. Conclusion

This work established the deformation mechanism of laser-welded P91 joints by considering effects of both heterogeneous residual stress and localised microstructures. The residual stress distribution across the narrow sub-regions of the joints was quantified and cross-validated, where the peak residual tensile stress (~150 MPa) is found in loading direction at the FZ/HAZ interface, balanced by compressive residual stress on both sides. While microstructural strengthening phenomenon is overwhelming in tensile behaviour, residual stress effect in micro-hardness is much identical. The FZ and HAZ regions showed a higher yield strength, and the fracture occurred at the BM region. Whilst the weldment softs at the high temperature, the ductile and strain hardening effect increase. This observation is consistent with the fractographic analysis, which shows a greater presence of ductile fracture features at elevated temperatures.

5. Acknowledgements

The authors give thanks to the Karlsruhe Institute of Technology for providing the P91 plate for this study and Dr Simon Kirk (UKAEA) for his advice on laser welding. This work has been carried out within the framework of the EUROfusion Consortium, funded by the European Union via the Euratom Research and Training Programme (Grant Agreement No

101052200 — EUROfusion). Views and opinions expressed are however those of the author(s) only and do not necessarily reflect those of the European Union or the European Commission. Neither the European Union nor the European Commission can be held responsible for them. Dr Wang and Dr Gorley would also like to acknowledge the EPSRC grants (EP/W006839/1) and the UK Government Department for Business, Energy and Industrial Strategy for their time and resources. Dr Sui would like to acknowledge funding from the Royal Academy of Engineering under the Industrial Fellowships programme. Part of this work was supported by grants from the EPSRC project (EP/P001521/1). Dr Zhang would like to thank the National Measurement System Programme of the UK Government Department for Business, Energy and Industrial Strategy for financial support.

6. Reference

- [1] Lässer R, Baluc N, Boutard JL, et al. Structural materials for DEMO: The EU development, strategy, testing and modelling. Fusion Engineering and Design. 2007;82:511–520.
- [2] Andreani R, Diegele E, Laesser R, et al. The European integrated materials and technology programme in fusion. Journal of Nuclear Materials. North-Holland; 2004. p. 20–30.
- [3] Kirk S, Suder W, Keogh K. Laser Welding of P91 & EUROFER97 steels for fusion reactor coolant pipes. 2016.
- [4] Pintsuk G, Aiello G, Dudarev SL, et al. Materials for in-vessel components. Fusion Engineering and Design. 2022;174:112994.
- [5] Pandey C, Giri A, Mahapatra MM. Evolution of phases in P91 steel in various heat treatment conditions and their effect on microstructure stability and mechanical properties. Materials Science and Engineering A. 2016;664.
- [6] Kirk S, Suder W, Keogh K, et al. Laser welding of fusion relevant steels for the European DEMO. Fusion Engineering and Design. 2018;
- [7] Tanigawa H, Maruyama T, Noguchi Y, et al. Laser welding to expand the allowable gap in bore welding for ITER blanket hydraulic connection. Fusion Engineering and Design. 2015;98–99:1634–1637.
- [8] Withers PJ. Residual stress and its role in failure. Reports on Progress in Physics [Internet]. 2007 [cited 2020 Dec 30];70:2211–2264. Available from: http://stacks.iop.org/0034-4885/70/i=12/a=R04?key=crossref.595db726860ce6f8a244246e705396a0.
- [9] Wang Y, Kannan R, Li L. Insight into Type IV cracking in Grade 91 steel weldments. Mater Des. 2020;190:108570.
- [10] Zhang S, Melfi T, Narayanan BK. Effects of precipitates on mechanical properties of P91 submerged arc welds. Science and Technology of Welding and Joining. 2016;
- [11] Vidyarthy RS, Dwivedi DK. Microstructural and mechanical properties assessment of the P91 A-TIG weld joints. J Manuf Process. 2018;31.
- [12] Bi T, Deng D, Tong Y, et al. Investigation of Influence of Phase Transformation on Welding Residual Stress in P91 Steel. Proceedings of the WSE2013. 2013;

- [13] Ruiz-Moreno A, Hähner P, Fumagalli F, et al. Stress-strain curves and derived mechanical parameters of P91 steel from spherical nanoindentation at a range of temperatures. Mater Des. 2020;194:108950.
- [14] Sauraw A, Sharma AK, Fydrych D, et al. Study on microstructural characterization, mechanical properties and residual stress of gtaw dissimilar joints of p91 and p22 steels. Materials. 2021;14.
- [15] Park HK, Ameyama K, Yoo J, et al. Additional hardening in harmonic structured materials by strain partitioning and back stress. Mater Res Lett. 2018;6.
- [16] Ahn J, Chen L, He E, et al. Effect of filler metal feed rate and composition on microstructure and mechanical properties of fibre laser welded AA 2024-T3. J Manuf Process. 2017;25:26–36.
- [17] Yildirim C, Jessop C, Ahlström J, et al. 3D mapping of orientation variation and local residual stress within individual grains of pearlitic steel using synchrotron dark field X-ray microscopy. Scr Mater. 2021;197:113783.
- [18] Chen W, Voisin T, Zhang Y, et al. Microscale residual stresses in additively manufactured stainless steel. Nat Commun. 2019;10.
- [19] Oliveira JP, Fernandes FMB, Miranda RM, et al. Residual stress analysis in laser welded NiTi sheets using synchrotron X-ray diffraction. Mater Des. 2016;100.
- [20] Withers PJJ, Bhadeshia HKDHKDH. Residual stress. Part 1 Measurement techniques. Materials Science and Technology [Internet]. 2013 [cited 2019 May 22];17:355–365. Available from: http://www.tandfonline.com/doi/full/10.1179/026708301101509980.
- [21] Paddea S, Francis JA, Paradowska AM, et al. Residual stress distributions in a P91 steel-pipe girth weld before and after post weld heat treatment. Materials Science and Engineering A. 2012;534:663–672.
- [22] Kundu A, Bouchard PJ, Kumar S, et al. Residual stresses in P91 steel electron beam welds. Science and Technology of Welding and Joining. 2012;18.
- [23] Yaghi AH, Hyde TH, Becker AA, et al. Finite element simulation of welding and residual stresses in a P91 steel pipe incorporating solid-state phase transformation and post-weld heat treatment. [cited 2022 Mar 14]; Available from: https://journals.sagepub.com/doi/abs/10.1243/03093247jsa372.
- [24] Kumar S, Kundu A, Venkata KA, et al. Residual stresses in laser welded ASTM A387 Grade 91 steel plates. Materials Science and Engineering A [Internet].

- [25] Javadi Y, Smith MC, Abburi Venkata K, et al. Residual stress measurement round robin on an electron beam welded joint between austenitic stainless steel 316L(N) and ferritic steel P91. International Journal of Pressure Vessels and Piping. 2017;154:41–57.
- [26] Kim S-H, Kim J-B, Lee W-J. Numerical prediction and neutron diffraction measurement of the residual stresses for a modified 9Cr–1Mo steel weld. J Mater Process Technol. 2009;209:3905–3913.
- [27] bin Zhu, Yiqiang Wang, Jiří Dluhoš, et al. A novel pathway for multiscale high-resolution time-resolved residual stress evaluation of laser-welded Eurofer97. Sci Adv [Internet]. 2022;8:eabl4592. Available from: https://doi.org/10.1126/sciadv.abl4592.
- [28] Mainprice D, Hielscher R, Schaeben H. Calculating anisotropic physical properties from texture data using the MTEX open-source package. Geol Soc Spec Publ [Internet]. 2011 [cited 2021 Jun 1];360:175–192. Available from: https://sp.lyellcollection.org/content/360/1/175.
- [29] Roebuck B, Bennett EG, Dickson A. The measurement of uncertainty in grain size distribution. Interlaboratory exercise part 1-reference images. National Physical Lab.; 1999.
- [30] Sui T, Lunt AJG, Baimpas N, et al. Understanding nature's residual strain engineering at the human dentine-enamel junction interface. Acta Biomater. 2016;32.
- [31] Salvati E, Sui T, Korsunsky AM. Uncertainty quantification of residual stress evaluation by the FIB-DIC ring-core method due to elastic anisotropy effects. Int J Solids Struct. 2016;87:61–69.
- [32] Archie F, Mughal MZ, Sebastiani M, et al. Anisotropic distribution of the micro residual stresses in lath martensite revealed by FIB ring-core milling technique. Acta Mater [Internet]. 2018;150:327–338. Available from: https://www.sciencedirect.com/science/article/pii/S1359645418302246.
- [33] Lee YH, Kwon D. Measurement of residual-stress effect by nanoindentation on elastically strained (1 0 0) W. Scr Mater. 2003;49:459–465.
- [34] Lee YH, Kwon D. Estimation of biaxial surface stress by instrumented indentation with sharp indenters. Acta Mater. 2004;52:1555–1563.

- [35] Pharr GM. An improved technique for determining hardness and elastic modulus using load and displacement sensing indentation experiments. J Mater Res. 1992;7:1564–1583.
- [36] Student REU, Cintr R, Mentor REU, et al. Strain Measurements with the Digital Image Correlation System Vic-2D. Image (Rochester, NY). 2008;
- [37] Manugula VL, Rajulapati K v., Reddy GM, et al. Role of evolving microstructure on the mechanical properties of electron beam welded ferritic-martensitic steel in the as-welded and post weld heat-treated states. Materials Science and Engineering A. 2017;698.
- [38] Wang L, Li M, Almer J. Investigation of deformation and microstructural evolution in Grade 91 ferritic—martensitic steel by in situ high-energy X-rays. Acta Mater. 2014;62:239–249.
- [39] Suresh S, Giannakopoulos AE. A new method for estimating residual stresses by instrumented sharp indentation. Acta Mater. 1998;46:5755–5767.
- [40] Greco A, Sgambitterra E, Furgiuele F. A new methodology for measuring residual stress using a modified Berkovich nano-indenter. Int J Mech Sci. 2021;207.
- [41] Moon JH, Baek SM, Lee SG, et al. Effects of residual stress on the mechanical properties of copper processed using ultrasonic-nanocrystalline surface modification. Mater Res Lett [Internet]. 2019;7:97–102. Available from: https://www.tandfonline.com/doi/full/10.1080/21663831.2018.1560370.
- [42] Ma X, Higgins W, Liang Z, et al. Exploring the origins of the indentation size effect at submicron scales. Proc Natl Acad Sci U S A. 2021;118.
- [43] Cerjak H, Mayr P. Creep strength of welded joints of ferritic steels. Creep-Resistant Steels. Elsevier; 2008. p. 472–503.
- [44] Abburi Venkata K, Truman CE, Coules HE, et al. Applying electron backscattering diffraction to macroscopic residual stress characterisation in a dissimilar weld. J Mater Process Technol. 2017;241.
- [45] Raath ND, Norman D, McGregor I, et al. Effect of Weld Schedule on the Residual Stress Distribution of Boron Steel Spot Welds. Metallurgical and Materials Transactions A. 2017;48:2900–2914.
- [46] González-Velázquez JL. Fractography and Failure Analysis. Cham: Springer International Publishing; 2018.

- [47] Pandey C, Mahapatra MM, Kumar P, et al. Effect of strain rate and notch geometry on tensile properties and fracture mechanism of creep strength enhanced ferritic P91 steel. Journal of Nuclear Materials. 2018;498:176–186.
- [48] Saini N, Pandey C, Mahapatra MM, et al. A comparative study of ductile-brittle transition behavior and fractography of P91 and P92 steel. Eng Fail Anal [Internet]. 2017 [cited 2022 Aug 31];81:245–253. Available from: https://www.researchgate.net/publication/317825243_A_comparative_study_of _ductile-brittle_transition_behavior_and_fractography_of_P91_and_P92_steel.
- [49] Blach J, Falat L, Ševc P. Fracture characteristics of thermally exposed 9Cr–1Mo steel after tensile and impact testing at room temperature. Eng Fail Anal. 2009;16:1397–1403.